JACS
JOURNAL OF THE AMERICAN CHEMICAL SOCIETY
Communication
pubs.acs.org/JACS

Long-Distance Charge Carrier Funneling in Perovskite Nanowires Enabled by Built-in Halide Gradient

Wenming Tian,[†] Jing Leng,[†] Chunyi Zhao, and Shengye Jin*

State Key Laboratory of Molecular Reaction Dynamics and Collaborative Innovation Center of Chemistry for Energy Materials (iChEM), Dalian Institute of Chemical Physics, Chinese Academy of Sciences, 457 Zhongshan Road, Dalian, China, 116023

Supporting Information

ABSTRACT: The excellent charge carrier transportation in organolead halide perovskites is one major contributor to the high performance of many perovskite-based devices. There still exists a possibility for further enhancement of carrier transportation through nanoscale engineering, owing to the versatile wet-chemistry synthesis and processing of perovskites. Here we report the successful synthesis of bromide-gradient $CH_3NH_3PbBr_xI_{3-x}$ single-crystalline nanowires (NWs) by a solid-to-solid ion exchange reaction starting from one end of pure $CH_3NH_3PbI_3$ NWs, which was confirmed by local photoluminescence (PL) and energy dispersive X-ray spectroscopy (EDS) measurements. Due to the built-in halide gradient, the long-distance carrier transportation was driven by the energy funnel, rather than the spontaneous carrier diffusion. Indeed, local PL kinetics demonstrated effective charge carrier transportation only from the high-bandgap bromide-rich region to the low-bandgap iodine-rich region over a few micrometers. Therefore, these halide gradient NWs might find applications in various optoelectronic devices requiring long-distance and directional delivery of excitation energy.

Organolead halide perovskites $MAPbX_3$ ($MA = CH_3NH_3^+$; $X = Cl^-, Br^-, I^-$) have emerged as attractive materials for photovoltaic[1−6] and optoelectronic devices.[7−12] In perovskite-based devices, a long-distance carrier diffusion is essential to high device performance. Diffusion lengths up to micrometers have been reported in both polycrystalline and single-crystal perovskites.[13−17] In addition to utilizing the intrinsic transport properties of perovskites, the versatile wet-chemistry synthesis and processing of perovskites allow further enhancement of carrier transportation through nanoscale engineering. One of the strategies is recently reported carrier transportation driven by the bandgap energy gradient in alloyed perovskite materials.[18−20] For example, Kamat et al. and Choi et al. have reported carrier transportation in halide-gradient $CsPbBr_xI_{3-x}$ and $MAPbBr_xI_{3-x}$ thin films fabricated by a halide ion exchange reaction,[18,19] where the carriers were found to flow directionally from the high-bandgap bromide-rich region to the low-bandgap iodide-rich region across the film. This carrier-funneling was believed to facilitate carrier extraction at perovskite/electrode interfaces when applied in solar cells. Meanwhile, Sargent and co-workers also reported hybrid two-dimensional (2D) perovskite films comprising grains with different bandgap energy to funnel the charge carriers to the lowest-bandgap emitting sites and achieved significantly improved light-emitting performance.[20] These pioneer works opened a new avenue to manipulate carrier conveyance by tailoring the perovskite composition. However, in comparison with the intrinsic carrier diffusion, the carrier transportation distance and efficiency to be achieved by this compositional manipulation still remain unknown. It is therefore essential to develop a deep understanding of this energy-driven carrier transportation in the well-defined perovskite structure to facilitate their application in practical devices.

Perovskite single crystals have been designated as standard materials to explore the intrinsic properties of perovskites.[15,17,21] In our previous work, we have successfully demonstrated the application of a time-resolved and PL-scanned imaging microscopy technique in studying carrier diffusion dynamics in perovskite single-crystalline nanowires (NWs) and nanoplates (NPs).[16] We therefore aimed to fabricate a halide-gradient $MAPbBr_xI_{3-x}$ NW comprising a bromide-rich region (high-bandgap) at one side of the wire and an iodide-rich region (low bandgap) at the other (Figure 1)

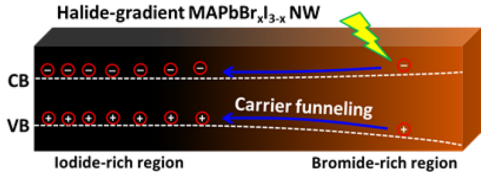

Figure 1. Halide-gradient $MAPbBr_xI_{3-x}$ perovskite nanowires (NW) comprising a bromide-rich region and an iodide-rich region. By changing the bandgap energy, the gradient distribution of halide ion forms an energy funnel along the NW, which drives carriers to transport from the high-bandgap bromide-rich region to the low-bandgap iodide-rich region.

such that the energy difference between them can drive the unidirectional transportation of charge carriers. It has been shown that perovskite bulk films with halide gradient distribution can be prepared by a solid-to-solution or solid-to-gas ion exchange reaction.[18,19] However, using these methods to form a halide gradient in individual perovskite NWs can be difficult.

Herein, we developed a "solid-to-solid" halide exchange reaction and successfully synthesized halide-gradient

Received: October 7, 2016
Published: December 30, 2016

DOI: 10.1021/jacs.6b10512
J. Am. Chem. Soc. 2017, 139, 579−582

$MAPbBr_xI_{3-x}$ perovskite NWs by directly contacting $MAPbI_3$ NWs with bulk $MAPbBr_3$ single crystals. The gradient distribution of bromide ion in individual $MAPbBr_xI_{3-x}$ NWs was confirmed by energy dispersive X-ray spectroscopy (EDS) elemental mapping and local emission spectra. Using time-resolved PL imaging and kinetics measurements, we observed several-micrometers unidirectional charge carrier transportation from the bromide-rich region to the iodide-rich region. In comparison with the intrinsic carrier diffusion, the carrier transportation driven by the bandgap energy gradient exhibited superior ability in directional carrier transfer, making these NWs ideal candidates for applications in long-distance photon-energy delivery and nanoscale optoelectronics.

We first grew $MAPbI_3$ single-crystal NWs on a glass slide by following the previously reported methods (see Supporting Information (SI) for details).[11] These NWs are 5 to 10 μm in length and a few hundreds of nanometers in rectangular width (Figure S1). In order to synthesize halide-gradient $MAPbBr_xI_{3-x}$ NWs, preprepared pure $MAPbBr_3$ single crystals (2−3 mm in size, see SI for details) were scattered on the top of the as-grown $MAPbI_3$ NW substrate (Figure S2). Since most $MAPbI_3$ NWs grew almost perpendicularly to the substrate (Figure S1), they have only one end in contact with the large $MAPbBr_3$ single crystals, where the interfacial halide exchange reaction occurs. Unlike the fast anion exchange in solution,[12,22−25] we found that this solid-to-solid halide exchange reaction took at least 15 days.

After the anion exchange reaction, we carefully removed the $MAPbBr_3$ single crystals and transported the NWs to a clean glass coverslip. Scanning electronic microscopy (SEM) and energy dispersive X-ray spectroscopy (EDS) were first used to examine the morphology and compositional distribution in the NWs. Figure 2a shows the SEM image and EDS mapping of Pb, Br, and I elements in a typical individual $MAPbBr_xI_{3-x}$ NW. Unlike the homogeneous distribution of lead over the entire NW, the iodide and bromide elements both show gradient distributions with the concentration decreasing in opposite directions along the wire. Such gradient distribution is not observed in pure $MAPbI_3$ and $MAPbBr_3$ NWs (Figure S3). These results confirm that the halide exchange reaction indeed started from one end of the NW and formed both bromide-rich and iodide-rich regions in the same NW. Because replacing the iodide anion by the bromide anion increases the bandgap energy, it is expected that a blue shift in the emission should be observed. We therefore compared the local emission spectra extracted from the two ends and center in the same $MAPbBr_xI_{3-x}$ NW (Figure 2b). A gradual blue shift from the iodide-rich region (peak at 752 nm) to the bromide-rich region (peak at ∼711 nm) is observed, further confirming the formation of the halide ion gradient within the single NW. Based on the blue shift in the emission spectra, the maximum energy difference is calculated to be ΔE = ∼0.09 eV. This energy difference is higher than room temperature thermal energy (∼0.025 eV) and hence is sufficient to create an effective energy funnel within the NW. Among >100 examined NWs, we observed ∼50% of NWs showing clear gradient distribution of the halide ion. More examples of EDS and spectra measurements in other gradient $MAPbBr_xI_{3-x}$ NWs are shown in Figure S4.

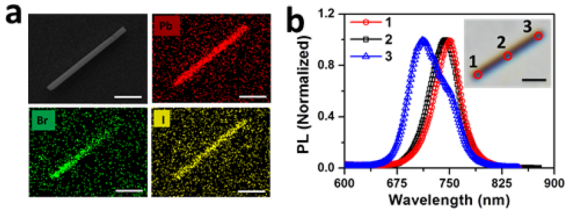

Figure 2. (a) SEM image and EDS mapping of lead (Pb), bromine (Br), and iodine (I) elements in a typical gradient $MAPbBr_xI_{3-x}$ NW, showing a gradient distribution of halide ions along the NW. (b) Local emission spectra collected (collection spot <1 μm in diameter) at the iodide-rich region (position 1), the central area (position 2), and bromide-rich region (position 3) in the same $MAPbBr_xI_{3-x}$ NW as in panel (a). The inset is the optical image of the NW. The scale bars are 2 μm. The blue-shifted spectra are due to the increase of bandgap energy induced by the mixture of bromide ion in the perovskite.

In order to understand the effect of the energy funnel on the carrier transportation dynamics, we collected the PL images and local PL kinetics of individual perovskite NWs using time-resolved and PL-scanned imaging microscopy (see Figure S5). The NWs were excited homogeneously (500 nm, 1 MHz, 67.8 nJ/cm^2/pulse) over the entire particle, and the PL intensity was recorded by scanning the PL collection spot (diffraction limited size) on the NW to construct the PL images. Coupled with the TCSPC module, the local PL kinetics at any positions in the NW can be extracted. Under a homogeneous excitation, net carrier diffusion is absent due to the lack of carrier density gradient. The pure $MAPbI_3$ NW thus exhibits a uniform distribution in both PL intensity (Figure 3a) and local PL dynamics (Figure 3b). In contrast, the $MAPbBr_xI_{3-x}$ NW (ΔE = ∼0.07 eV as determined in Figure S6) shows a gradient distribution in PL intensity, which decreases distinctly from one end to the other (Figure 3c). The local emission spectra (Figure S6) identify the bright region in the iodide-rich side

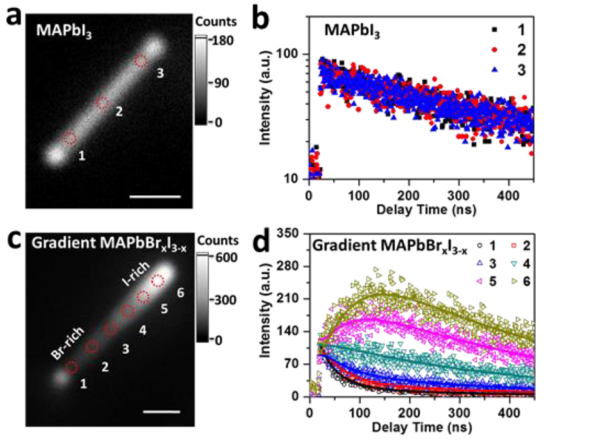

Figure 3. (a and c) Time-resolved PL intensity images of a $MAPbI_3$ NW and a gradient $MAPbBr_xI_{3-x}$ NW under a homogeneous excitation at 500 nm (1 MHz, 67.8 nJ/cm^2/pulse). (b and d) Comparisons of the local PL kinetics extracted from the indicated positions (PL collection spot <1 μm in diameter) for the $MAPbI_3$ NW (position 1−3) and the gradient $MAPbBr_xI_{3-x}$ NW (position 1−6). The scale bars are 2 μm. The $MAPbI_3$ NW exhibits a uniform distribution in both PL intensity and kinetics, while the gradient $MAPbBr_xI_{3-x}$ NW shows much higher PL intensity in the iodide-rich region and dramatically changed local PL kinetics, which is attributed to the carrier transportation from the bromide-rich region to the iodide-rich region driven by the bandgap energy gradient. The solid lines are the fits of the kinetics by the carrier transportation model (eqs S1 and S2), yielding the charge mobility and diffusion coefficient of the NW.

DOI: 10.1021/jacs.6b10512
J. Am. Chem. Soc. 2017, 139, 579−582

and the dark region in the bromide-rich side in the NW. In Figure 3d we also compared the local PL kinetics extracted from different positions (spots 1 to 6 in Figure 3c) in the gradient NW. These kinetics show fast decays in the bromide-rich region, and the decays become slower as the examining position move toward the iodide-rich region where the kinetics is finally accompanied by the formation of a rising component within 100 ns after excitation.

In our control experiments, we synthesized $MAPbBr_xI_{3-x}$ NWs with a uniform mixture of the bromide ion. In such NWs, the PL intensity and kinetics are also homogeneously distributed (Figure S7), and the PL lifetimes are found to be >200 ns. Furthermore, we also performed excitation intensity dependent transient PL measurements on an evenly Br-doped $MAPbBr_xI_{3-x}$ NW (fabricated by an ion-exchange reaction). The charge recombination constants are similar to those in the $MAPbI_3$ NW (see Figure S8). These results suggest that the fast decays in the bromide-rich region in the gradient $MAPbBr_xI_{3-x}$ NW cannot be attributed to the fast carrier recombination by trapping states introduced in the ion exchange reaction.

We attribute the nonuniform PL intensity and kinetics in the gradient $MAPbBr_xI_{3-x}$ NW to the carrier flow from bromide-rich region to the iodide-rich region driven by the energy funnel in the NW. The fast PL decay in the bromide-rich region is due to the flow-out of carriers to the iodide-rich region, where the flow-in of carriers generates a rising component in PL kinetics. Consequently, this carrier flow accumulates the carriers in the iodide-rich region, resulting in higher PL intensity. The electronic structure of perovskite has indicated that the halide dominates in contribution to the valence band.[26] Replacing the iodide with the bromide ion mainly raises the valence band to higher energy levels. Within the bromide gradient in the $MAPbBr_xI_{3-x}$ NW, we anticipate that the energy funnel pushes the holes from the bromide-rich region to the iodide-rich region. However, the observation of PL (due to recombination of electrons and holes) on the gradient NW indicates that the transportation of holes likely pulls the electrons to move together by Coulombic attraction.

Figure 3d shows that the PL kinetics in the halide-gradient NW can be well described by numerically solving a carrier transportation model (eqs S1 and S2), which includes both carrier diffusion and funneling processes (see SI for the details). The global fit of the kinetics yields a charge mobility (μ) of ~41.5 $cm^2\ v^{-1}\ s^{-1}$ and an ambipolar diffusion coefficient (D) of ~1.2 $cm^2\ s^{-1}$ (see Table S1). The measured μ should be close to the hole mobility in the NW. These values are consistent with those reported in literature,[15−17] confirming the validity of the model.

To compare the efficiency of carrier delivery (number of carriers in total population that can transport over a specific distance) between the energy-driven carrier transportation and the spontaneous carrier diffusion, we also collected PL images of NWs with a focused laser excitation (500 nm, 1 MHz, 1.35 $\mu J/cm^2$/pulse). Under this condition, the PL emission from positions other than the excitation spot (~1 μm in diameter) indicates the carrier transportation in the NW.[16] In Figure 4a and b, we compared the PL images of a gradient $MAPbBr_xI_{3-x}$ NW and a pure $MAPbI_3$ NW upon excitation at one end of the wire. For the gradient $MAPbBr_xI_{3-x}$ NW (ΔE = ~0.06 eV as determined in Figure S9), the excitation at the bromide-rich region results in significantly higher PL intensity in the iodide-rich region that is away by a few micrometers, while, for the

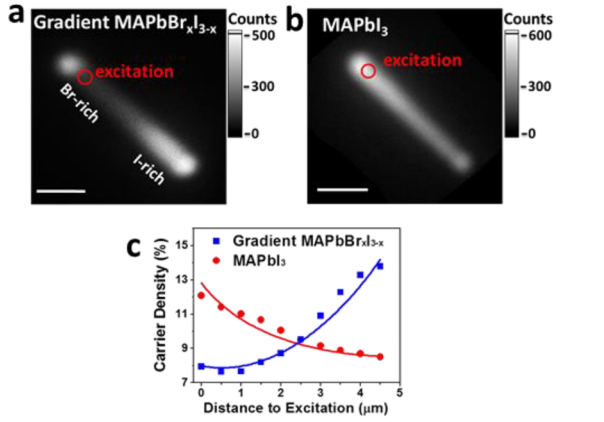

Figure 4. PL intensity images of (a) a gradient $MAPbBr_xI_{3-x}$ NW and (b) a $MAPbI_3$ NW excited with a focused laser beam (spot diameter <1 μm, 500 nm, 1 MHz, 1.35 $\mu J/cm^2$/pulse) at one end of the wire. The scale bars are 2 μm. (c) Plots of relative carrier density (in the percentage of total population) as a function of distance to the excitation spot for the NWs shown in panel a and b, indicating that carrier transportation driven by bandgap energy gradient in the gradient $MAPbBr_xI_{3-x}$ NW delivers more carriers to a distance >2 um than the diffusion in the $MAPbI_3$ NW. The solid lines are fits of the plots by eq S5 with the fitting parameters listed in Table S1.

pure $MAPbI_3$ NW, PL intensity remains largely at the excitation spot. Because PL intensity is proportional to n^2 (n is the carrier density),[27] we calculated and plotted the relative local carrier density as a function of distance to the excitation spot along the NWs (Figure 4c). These plots and the local PL kinetics in the NWs (Figure S10) can also be described by the carrier transportation model. In the gradient $MAPbBr_xI_{3-x}$ NW, carrier transportation driven by the energy funnel delivers ~60% of carriers over a distance of >2 μm; in contrast, diffusion driven by the density gradient transports only 45% of carriers to the same distance in the pure $MAPbI_3$ NW. Indeed, no matter where the gradient $MAPbBr_xI_{3-x}$ NW is excited, carriers always accumulate at the iodide-rich region (Figure S11). These results suggest that the energy gradient is the dominant driving force for carrier transportation in the gradient $MAPbBr_xI_{3-x}$ NW, which then ensures effective carrier transportation in only a one-way direction. These results promise the potential application of these NWs in light harvesting and long-distance energy delivery.

Finally, we investigated the stability of the compositional gradient in the NWs. In mixed halide perovskite, it has been shown that iodide and bromide ions segregate during photoirradiation.[28,29] This phenomenon was not observed in the gradient $MAPbBr_xI_{3-x}$ NWs under our experimental conditions. The halide-gradient in the NWs exhibits nice stability at the examined temperatures from 25 to 100 °C (Figure S12). Furthermore, we also frequently examined the local emission spectra at the bromide-rich and iodide-rich regions during a period of days. Although the NWs show an overall blue shift in the spectra probably due to the intrinsic degradation of perovskite materials, the spectral shift between the bromide-rich region and iodide-rich region and the ensuing directional carrier flow remain up to more than 50 days (see Figure S13). These results suggest the possibility of these gradient NWs for long-term use in practical applications.

In summary, we successfully fabricated halide compositional gradient $MAPbBr_xI_{3-x}$ perovskite NWs by a solid-to-solid halide exchange reaction. EDS mapping and PL spectra

DOI: 10.1021/jacs.6b10512
J. Am. Chem. Soc. 2017, 139, 579−582

measurements confirmed that the density of the mixed bromide anion gradually decreases from one end to the other, forming a bromide-rich region and iodide-rich region in single NWs. By raising the bandgap energy, the halide gradient produced an energy funnel in the NWs, which facilitated the transportation of charge carriers in a one-way direction over a few micrometers and accumulated carriers in the low-bandgap iodide-rich region. The effective carrier transportation driven by the energy funnel, along with other superior intrinsic photophysical properties (e.g., long carrier lifetime and strong light harvesting), implies the applications of the halide gradient $MAPbBr_xI_{3-x}$ NWs in photon energy delivery and nanoscale optoelectronics.

■ ASSOCIATED CONTENT

Supporting Information

The Supporting Information is available free of charge on the ACS Publications website at DOI: 10.1021/jacs.6b10512.

Sample preparations; experimental setup; additional PL, SEM, and EDS measurements (PDF)

■ AUTHOR INFORMATION

Corresponding Author

*sjin@dicp.ac.cn

ORCID

Shengye Jin: 0000-0003-2001-2212

Author Contributions

†These authors contributed equally.

Notes

The authors declare no competing financial interest.

■ ACKNOWLEDGMENTS

S.J. acknowledges the financial support from the MOST (2016YFA0200602) and the NSFC (21473192).

■ REFERENCES

(1) Kojima, A.; Teshima, K.; Shirai, Y.; Miyasaka, T. *J. Am. Chem. Soc.* **2009**, *131*, 6050−6051.

(2) Yang, B.; Dyck, O.; Poplawsky, J.; Keum, J.; Puretzky, A.; Das, S.; Ivanov, I.; Rouleau, C.; Duscher, G.; Geohegan, D.; Xiao, K. *J. Am. Chem. Soc.* **2015**, *137*, 9210−9213.

(3) Pazos-Outon, L. M.; Szumilo, M.; Lamboll, R.; Richter, J. M.; Crespo-Quesada, M.; Abdi-Jalebi, M.; Beeson, H. J.; Vrucinic, M.; Alsari, M.; Snaith, H. J.; Ehrler, B.; Friend, R. H.; Deschler, F. *Science* **2016**, *351*, 1430−1433.

(4) McMeekin, D. P.; Sadoughi, G.; Rehman, W.; Eperon, G. E.; Saliba, M.; Horantner, M. T.; Haghighirad, A.; Sakai, N.; Korte, L.; Rech, B.; Johnston, M. B.; Herz, L. M.; Snaith, H. J. *Science* **2016**, *351*, 151−155.

(5) Yang, W. S.; Noh, J. H.; Jeon, N. J.; Kim, Y. C.; Ryu, S.; Seo, J.; Seok, S. I. *Science* **2015**, *348*, 1234−1237.

(6) Zhou, H. P.; Chen, Q.; Li, G.; Luo, S.; Song, T. B.; Duan, H. S.; Hong, Z. R.; You, J. B.; Liu, Y. S.; Yang, Y. *Science* **2014**, *345*, 542−546.

(7) Liu, J.; Xue, Y.; Wang, Z.; Xu, Z. Q.; Zheng, C.; Weber, B.; Song, J.; Wang, Y.; Lu, Y.; Zhang, Y.; Bao, Q. *ACS Nano* **2016**, *10*, 3536−3542.

(8) Su, L.; Zhao, Z. X.; Li, H. Y.; Yuan, J.; Wang, Z. L.; Cao, G. Z.; Zhu, G. *ACS Nano* **2015**, *9*, 11310−11316.

(9) Tan, Z. K.; Moghaddam, R. S.; Lai, M. L.; Docampo, P.; Higler, R.; Deschler, F.; Price, M.; Sadhanala, A.; Pazos, L. M.; Credgington, D.; Hanusch, F.; Bein, T.; Snaith, H. J.; Friend, R. H. *Nat. Nanotechnol.* **2014**, *9*, 687−692.

(10) Li, F.; Ma, C.; Wang, H.; Hu, W.; Yu, W.; Sheikh, A. D.; Wu, T. *Nat. Commun.* **2015**, *6*, 8238.

(11) Zhu, H.; Fu, Y.; Meng, F.; Wu, X.; Gong, Z.; Ding, Q.; Gustafsson, M. V.; Trinh, M. T.; Jin, S.; Zhu, X. Y. *Nat. Mater.* **2015**, *14*, 636−642.

(12) Zhang, D.; Yang, Y.; Bekenstein, Y.; Yu, Y.; Gibson, N. A.; Wong, A. B.; Eaton, S. W.; Kornienko, N.; Kong, Q.; Lai, M.; Alivisatos, A. P.; Leone, S. R.; Yang, P. *J. Am. Chem. Soc.* **2016**, *138*, 7236−7239.

(13) Xiao, Z. G.; Dong, Q. F.; Bi, C.; Shao, Y. C.; Yuan, Y. B.; Huang, J. S. *Adv. Mater.* **2014**, *26*, 6503−6509.

(14) Deng, Y. H.; Peng, E.; Shao, Y. C.; Xiao, Z. G.; Dong, Q. F.; Huang, J. S. *Energy Environ. Sci.* **2015**, *8*, 1544−1550.

(15) Dong, Q.; Fang, Y.; Shao, Y.; Mulligan, P.; Qiu, J.; Cao, L.; Huang, J. *Science* **2015**, *347*, 967−970.

(16) Tian, W.; Zhao, C.; Leng, J.; Cui, R.; Jin, S. *J. Am. Chem. Soc.* **2015**, *137*, 12458−12461.

(17) Shi, D.; Adinolfi, V.; Comin, R.; Yuan, M.; Alarousu, E.; Buin, A.; Chen, Y.; Hoogland, S.; Rothenberger, A.; Katsiev, K.; Losovyj, Y.; Zhang, X.; Dowben, P. A.; Mohammed, O. F.; Sargent, E. H.; Bakr, O. M. *Science* **2015**, *347*, 519−522.

(18) Kim, M. C.; Kim, B. J.; Son, D. Y.; Park, N. G.; Jung, H. S.; Choi, M. *Nano Lett.* **2016**, *16*, 5756−5763.

(19) Hoffman, J. B.; Schleper, A. L.; Kamat, P. V. *J. Am. Chem. Soc.* **2016**, *138*, 8603−8611.

(20) Yuan, M.; Quan, L. N.; Comin, R.; Walters, G.; Sabatini, R.; Voznyy, O.; Hoogland, S.; Zhao, Y.; Beauregard, E. M.; Kanjanaboos, P.; Lu, Z.; Kim, D. H.; Sargent, E. H. *Nat. Nanotechnol.* **2016**, *11*, 872−877.

(21) Saidaminov, M. I.; Abdelhady, A. L.; Murali, B.; Alarousu, E.; Maulakov, V. M.; Peng, W.; Dursun, L.; Wang, L.; He, Y.; Maculan, G.; Goriely, A.; Wu, T.; Mohammed, O. F.; Bakr, O. M. *Nat. Commun.* **2015**, *6*, 7586.

(22) Akkerman, Q. A.; D'Innocenzo, V.; Accornero, S.; Scarpellini, A.; Petrozza, A.; Prato, M.; Manna, L. *J. Am. Chem. Soc.* **2015**, *137*, 10276−10281.

(23) Koscher, B. A.; Bronstein, N. D.; Olshansky, J. H.; Bekenstein, Y.; Alivisatos, A. P. *J. Am. Chem. Soc.* **2016**, *138*, 12065−12068.

(24) Nedelcu, G.; Protesescu, L.; Yakunin, S.; Bodnarchuk, M. I.; Grotevent, M. J.; Kovalenko, M. V. *Nano Lett.* **2015**, *15*, 5635−5640.

(25) Pellet, N.; Teuscher, J.; Maier, J.; Gratzel, M. *Chem. Mater.* **2015**, *27*, 2181−2188.

(26) Butler, K. T.; Frost, J. M.; Walsh, A. *Mater. Horiz.* **2015**, *2*, 228−231.

(27) Yamada, Y.; Nakamura, T.; Endo, M.; Wakamiya, A.; Kanemitsu, Y. *J. Am. Chem. Soc.* **2014**, *136*, 11610−11613.

(28) Hoke, E. T.; Slotcavage, D. J.; Dohner, E. R.; Bowring, A. R.; Karunadasa, H. I.; McGehee, M. D. *Chem. Sci.* **2015**, *6*, 613−617.

(29) Yoon, S. J.; Draguta, S.; Manser, J. S.; Sharia, O.; Schneider, W. F.; Kuno, M.; Kamat, P. V. *ACS Energy Lett.* **2016**, *1*, 290−296.

DOI: 10.1021/jacs.6b10512
J. Am. Chem. Soc. 2017, 139, 579−582